6/30/05

Dan Barnes (U. Col.), Dylan Brennan (MIT/GA), Eric Held (Utah St), Charlson Kim (U. Wisc.), Scott Kruger (TechX), Alexei Pankin (SAIC), Dalton Schnack (SAIC), Carl Sovinec (U. Wisc), and Philip Snyder (GA)

Report on completion of third quarter elm simulation milestone

3nrd Q (end of June 05)

Further extend the studies to include variation of the electron pressure along field line, and look for appropriate equilibrium for test cases.

During the previous (second) quarter we reported the development of a "realistic" equilibrium to be used in further ELM studies. This equilibrium had an internal q-profile and shape resembling common DIII-D discharges that exhibit ELMing behavior, and had an edge pedestal temperature of 600 eV. This equilibrium was confirmed to be unstable to ELMs with the ideal MHD code ELITE. It was then studied for linear stability using the resistive MHD model in the NIMROD code. The NIMROD code did not find any ELMs. Instead, an internal mode was found that resembled a resistive ballooning mode. The internal instability, and the ELM stability, were not understood.

Here we report the successful completion of the third quarter milestone, namely, *Further extend the studies to include variation of the electron pressure along field line, and look for appropriate equilibrium for test cases.*

We found that, within the resistive-viscous MHD model, the stability of the equilibrium studied during the second quarter ($T_{ped} = 600$ eV) is strongly influenced by isotropic viscosity. The unstable mode appears to have two components, one related to an internal ballooning-like structure, and another concentrated at the edge of the discharge. (These are not different modes, but merely characteristics of the eigenfunction for a given set of parameters.) For relatively large viscosity, the internal ballooning structure is dominant. The edge localized (ELM-like) component emerges as the viscosity is lowered, becoming dominant in the limit of vanishing viscosity. Intermediate values of the viscosity show a mixture of the ballooning and ELM-like structures.

The influence of the isotropic viscosity is measured by the magnetic Prandtl number. This is the ratio of the viscous and resistive diffusivities. Large Prandtl number indicates large viscosity relative to resistivity. small Prandtl number the opposite. In Figure 1 we plot the linear growth rate of the $n = 10$ mode for the case with $T_{ped} = 600$ eV, as a function of the magnetic Prandtl number, Pr, for several values of the Lundquist number, S. (All cases were run with a small isotropic thermal diffusivity of $\kappa = 1\ \mathrm{m}^2/\mathrm{sec}$.) In all cases, there is a clear change in the growth rate around Pr ~$O(1)$. This indicates the transition from the internal mode at large Pr to the edge localized mode at small Pr. (The results report during the second quarter had Pr = 10^3. Clearly, the large viscosity was the

reason that the edge localized mode was not seen.) The lateral shift in the curves shown in Figure 1 suggests that the mode may be influenced by the magnitude of the viscous diffusivity alone, rather than by Pr itself. The isolated points at Pr = 10^{-3} for the two largest values of *S* indicate that the growth rate of the edge localized mode is independent of the resistivity, in the limit of large resistivity. This suggests that the mode has ideal MHD origins, in agreement with the results of ELITE. The growth rates obtained by ELITE and NIMROD for this mode are in good agreement. We have not yet studied the scaling of the growth rate of the internal mode (at large Pr) with *S*. This study is being performed, and will be reported in the fourth quarter.

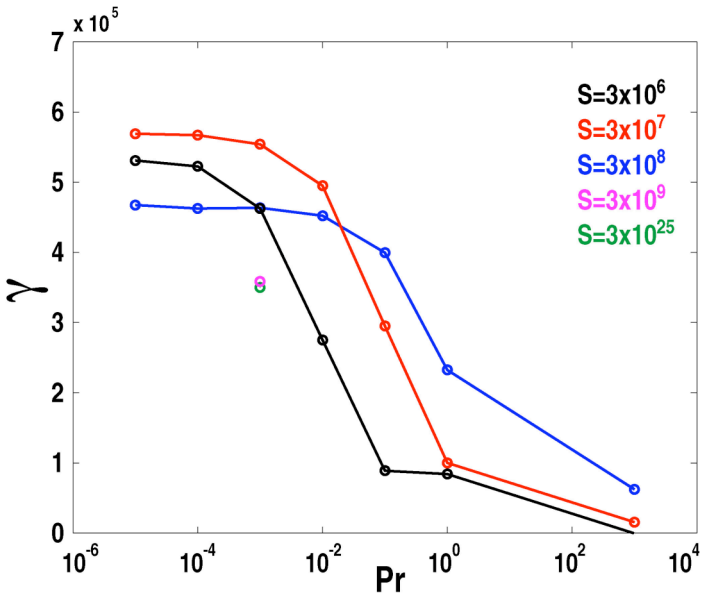

Figure 1. Growth rate (sec^{-1}) of the $n = 10$ mode vs. Prandtl number, for different values of the Lundquist number, for the equilibrium with $T_{ped} = 600$ eV. For small Prandtl number (small viscosity) the modes show an edge localized (ELM) structure. The resistive ballooning structure emerges at large Prandtl number. The region near Pr = 1 shows a mixed structure. All calculations were performed with isotropic thermal diffusivity of $\kappa = 1 \ m^2/sec$.

The large linear growth rate of the edge localized mode for the case of $T_{ped} = 600$ eV and low Pr ($\gamma\tau_A = 0.36$) indicates that this equilibrium may be well be well beyond the ideal linear stability boundary, and is therefore unlikely to exist under experimental conditions. We were thus motivated to construct a sequence of equilibria with successively decreasing pedestal temperature between 700 eV and 100 eV. These equilibria are shown in Figure 2. Note that the case with $T_{ped} = 100$ eV has essential no edge pedestal

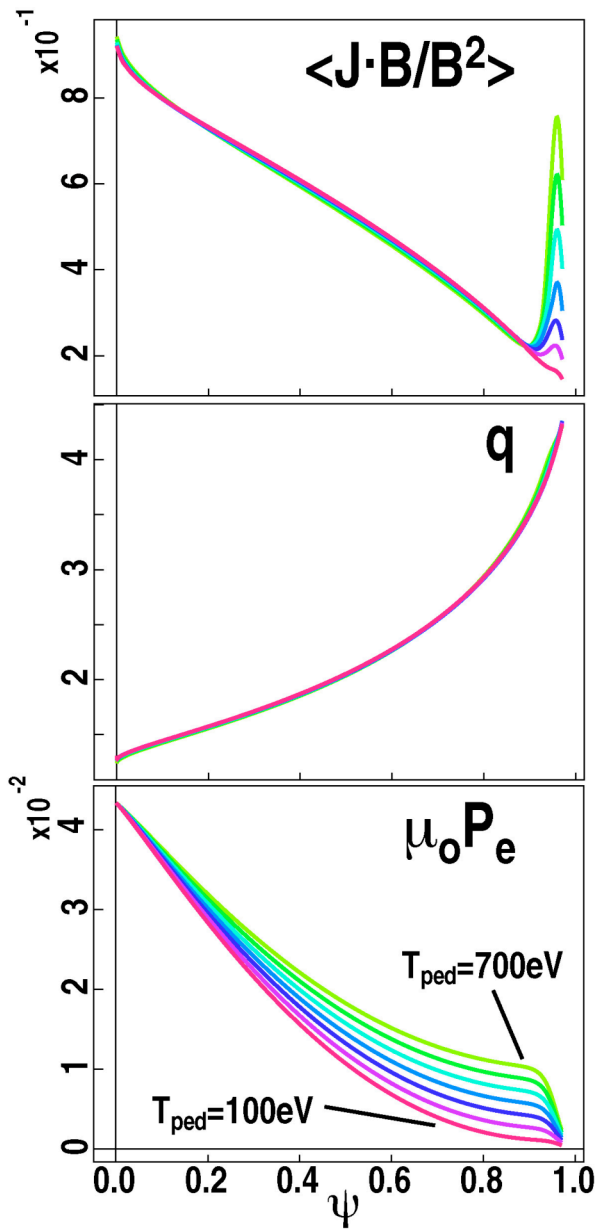

Figure 2. Sequence of DIII-D-like equilibria with successively decreasing pedestal temperature, but similar cross sectional shape. The top figure shows the parallel current profiles, the middle figure shows the *q*-profiles, and the bottom figure shows the temperature profiles. All profiles are functions of the equilibrium flux.

We have studied the linear stability of this family of equilibria with Pr = 10^{-3}, well below the transition indicated in Figure 1. The results are shown in Figure 3, where we plot the growth rate for modes with $n = 1$, 10, 20, and 30 versus T_{ped} for $S = 3.7 \times 10^8$ (again with isotropic thermal diffusivity of 1 m^2/sec). We note a transition between the ELM and the internal mode (IM), similar to that observed as a function of the Prandtl number, as the pedestal temperature is lowered. The $n = 1$ mode is stable for the lowest pedestal temperature.

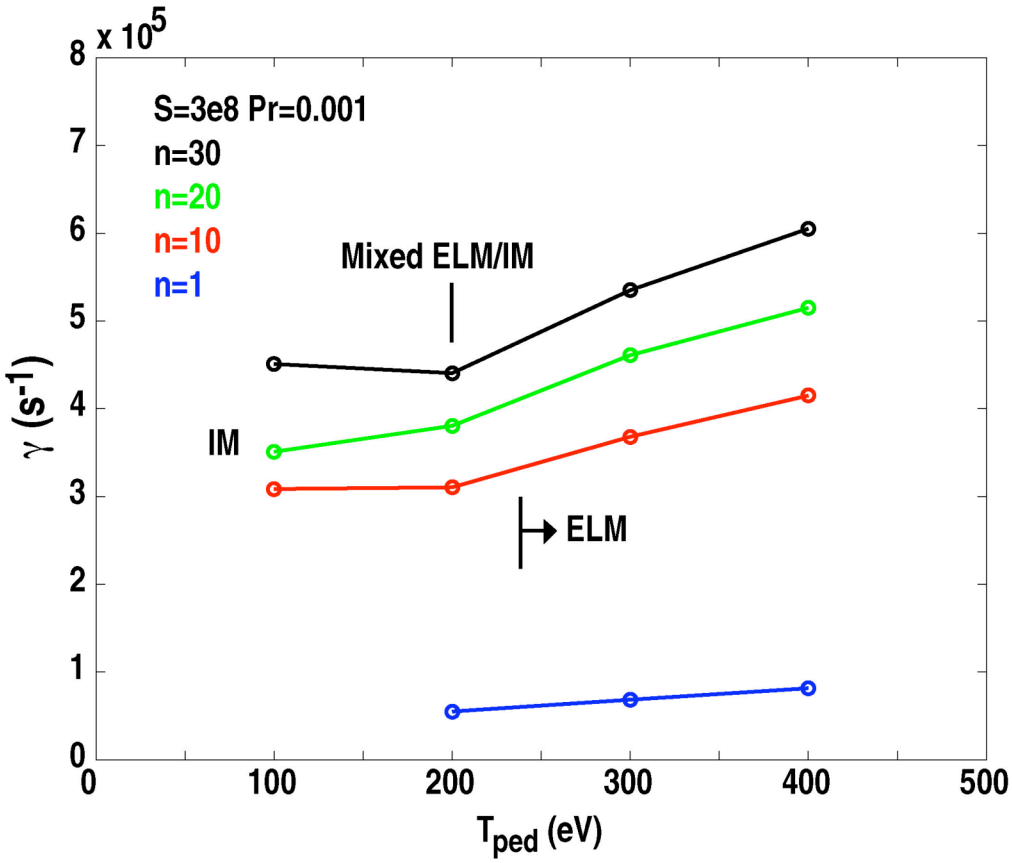

Figure 3. Linear growth rate for the n = 1, 10, 20, and 30 modes for the sequence of equilibria shown in Figure 2. For large pedestal temperatures, the mode is localized at the edge. This ELM-like component disappears as the pedestal is reduced, and the unstable mode becomes the internal mode (IM) reported in the second quarter. This transition is similar to the transition that occurs as a function of Pr (see Figure 1).

The transition of mode structure between the IM and the ELM is shown Figure 4, where we plot the eigenfunction for the electron temperature for the cases with pedestal temperatures of 100 eV, 200 eV, and 400 eV. The mode for the 100 eV has a dominant component that is resonant inside the separatrix, typical of the IM. The mode for the 400 eV case is clearly localized at the edge. At 200 eV, the mode shows an admixture of both structures. A similar transition in structure occurs at Pr ~ $O(1)$, as seen in Figure 1.

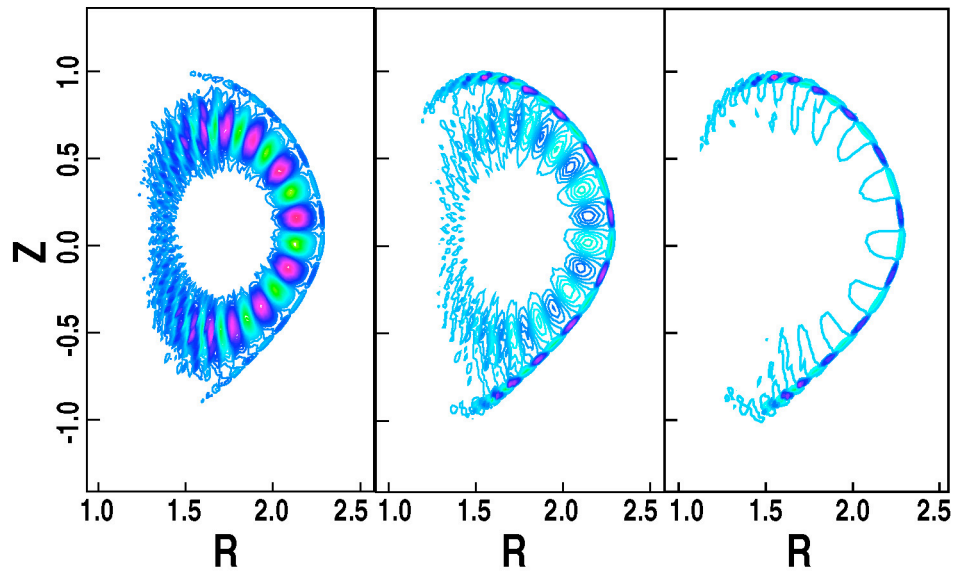

Figure 4. From left to right, linear eigenfunctions of the electron temperature for the $n = 10$ mode, for equilibria with pedestal temperatures of 100 eV, 200 eV, and 400 eV, respectively. The figure on the left (100 eV) is typical of the IM (internal mode), while the structure on the right (400 eV) is typical of the ELM. The central figure (200 eV) is an admixture of both types. A similar transition occurs as a function of Pr (see Figure 1).

The growth rates of the unstable modes found with NIMROD (with visco-resistive MHD and isotropic thermal diffusivity) in these equilibria increase monotonically with n, through $n = 40$. Ideal MHD calculations with ELITE show a fall-off at high-n. *We do not yet understand this qualitative difference between NIMROD and ELITE.*

There are theoretical indications using extended MHD that stabilization should occur at some moderate value of n. We have investigated three possible extensions to the NIMROD MHD model: *anisotropic thermal diffusivity*, *parallel* (as opposed to isotropic) *viscosity*, and *two-fluid* and *finite-Larmor radius (FLR) effects*. Preliminary results of these studies are reported below.

The effect of *anisotropic thermal diffusivity* ($\kappa_{\|}/\kappa_{\perp} >> 1$) is to flatten the temperature in the direction parallel to the magnetic field lines much faster than across them. Physically, this may be the result of collisions, free streaming by electrons, or parallel sound waves. In NIMROD this is modeled as an anisotropic (Braginskii) diffusion operator. In any case, it accounts for some *effects of pressure variations along the field lines*, and therefore meets the criteria for the third quarter milestone.

The growth rate is found to decrease with increasing anisotropy, with complete stabilization at $\kappa_{\|}/\kappa_{\perp} = 10^8$. The effect of anisotropic thermal diffusivity on linear stability is illustrated in Figure 5, where we plot the linear growth rate as a function of n for the case of $T_{ped} = 400$ eV, $S = 3.7 \times 10^8$, $\mathrm{Pr} = 10^{-3}$, and $\kappa_{\|}/\kappa_{\perp} = 10^7$. (For comparison with the results reported above, all cases were run with $\kappa_{\perp} = 1\ \mathrm{m}^2/\mathrm{sec}$.) The

growth rate now peaks at about $n = 20$, and continues decreasing to $n = 40$. (Higher toroidal mode numbers have not been studied.) The shorter wavelengths are more strongly affected by the parallel diffusivity, as is to be expected.

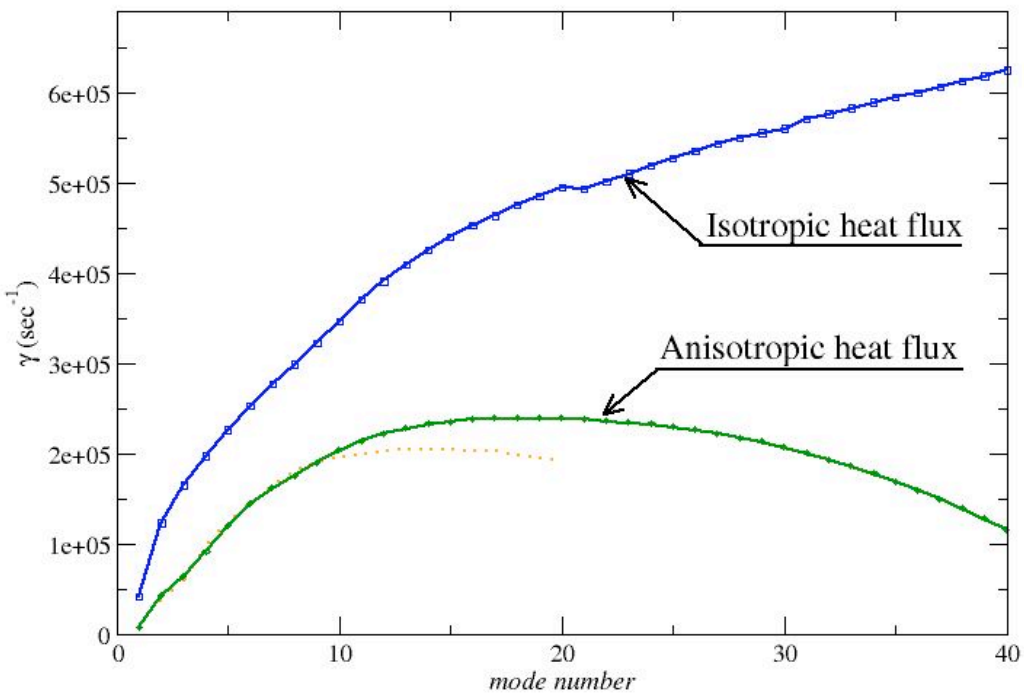

Figure 5. Linear growth rate as a function of toroidal mode number n, for the case with $T_{ped} = 400$ eV, $S = 3.7 \times 10^8$, $\Pr = 10^{-3}$, and $\kappa_{\|} / \kappa_{\perp} = 10^7$. The growth rate peaks near $n = 20$, and then decreases monotonically. (Complete stabilization is found for $\kappa_{\|} / \kappa_{\perp} = 10^8$.) The solid green curve was obtained with spatial resolution of 40 (radial) X 120 (poloidal) nodes. (For comparison, the solid blue curve was obtained with isotropic thermal diffusivity.) The dotted red curve was obtained 40 X 80 resolution, indicating the importance of spatially resolving modes with high-n. We emphasize that the points near $n = 40$ on the green curve are likely not spatially converged, and should be viewed with the appropriate skepticism.

In Figure5, the solid (green) curve was obtained with spatial resolution of 40 (radial) by 120 (poloidal) nodes, and bi-quartic finite elements. The dotted (red) curve was obtained with a mesh of 40 by 80 nodes. The deviation of these results at increasing n indicates the importance of adequate spatial resolution for high-n modes. It is therefore likely that the green curve is inaccurate at the highest n, and fully converged results my not even indicate a maximum in the growth rate. These important studies are underway. This has

implications for the non-linear computations required for the fourth quarter, and will be discussed later in this report.

Parallel transport appears to have a significant effect on the linear stability of edge localized modes in this family of equilibria. Obtaining physically realistic values of the parallel transport coefficients (parallel thermal diffusivity and viscosity), even in the edge of modern tokamaks, requires solution of the kinetic equation parallel to the magnetic field. This calculation of non-local parallel closures has been carried out for one of the equilibria studied here.

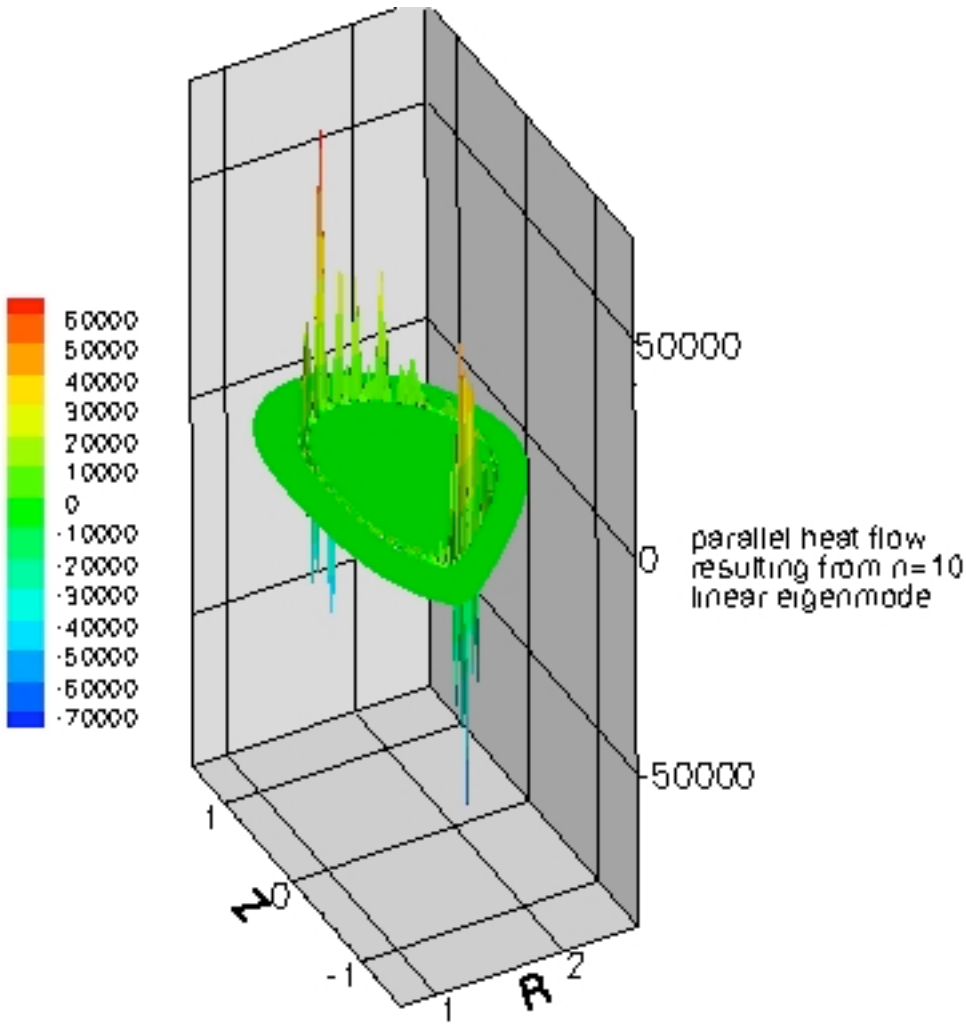

Figure 6. Parallel heat flow resulting from the $n = 10$ mode obtained with a non-local, parallel kinetic closure calculation. Note the concentration near the edge. The result is consistent with the use of $\kappa_{\|} / \kappa_{\perp} = 10^{7-8}$ in the Braginskii closure used in the NIMROD calculations (see Figure 5).

An important use of the quantitative, non-local parallel heat flow closure is to confirm that the ratio of $\kappa_{\|}/\kappa_{\perp}$ used in the numerically efficient Braginksii closure, is physically relevent. For these simulations, we calculated the resultant non-local, parallel heat flows

for the toroidal eigenmodes, $n = 5$, 10 and 20. A contour plot of the parallel heat flow response for the n=10 eigenmode is shown in Figure 6. Note that the heat flow, like the eigenmodes, is localized radially in the pedestal edge region. From this calculation, we inferred that at a value of $\kappa_{\|}/\kappa_{\perp}$ between 10^7 and 10^8, the Braginskii closure predicts a heat flow response comparable to that of the non-local closure. Hence, using anisotropic thermal conduction with $\kappa_{\|}/\kappa_{\perp} \sim 10^{7\text{-}8}$ to stabilize high toroidal mode numbers is physically relevant.

Additionally, a linear version of the non-local parallel ion stress, $\pi_{\|}$, has been implemented in order to test the linear effect of *parallel viscosity*. Using the same technique as above, we inferred a value for the parallel viscosity of approximately 10^4 which is to be used in linear calculations using NIMROD's local, Braginskii form for $\pi_{\|}$. The results, which are not reported here, show that parallel viscosity has little effect on growth rates or eigenmodes.

Linear two-fluid and FLR effects have been implemented into the NIMROD code, and studies of their effects on the linear stability of ELMs have begun. Two-fluid effects are represented by additional (Hall and diamagnetic) terms in Ohm's law, and FLR effects by the gyro-viscosity in the equation of motion. Both sets of terms (sometimes lumped together as "plasma drift effects") require special attention to the details of the algorithm to provide an efficient, stable method, and this effort is still underway. A few details are given below.

As their name implies, plasma drift effects induce propagation, and they alter the stability of MHD modes. In addition, two-fluid models have important dispersive waves, where frequencies are related to the square of the wavenumber, $\omega \sim k^2$. These properties change the mathematical character of the PDE system, and we have not found it practicable to retain only self-adjoint operators for large-Δt stabilization. One possibility is to use a time-centered implicit method. Another method that is being analysed and implemented retains the staggered differencing between **V** and other fields in the time domain and uses implicit operators at each step. Terms associated with drift and dispersive waves are made numerically stable by non-self-adjoint differential operators, while the operator for MHD waves is unchanged. Taking the limit of zero electron mass, the staggered time-discrete form of the two-fluid model with drift effects is:

$$\begin{aligned} m_i n^{j+1/2}\left(\frac{\Delta \mathbf{V}}{\Delta t} + \frac{1}{2}\mathbf{V}^j \cdot \nabla \Delta \mathbf{V} + \frac{1}{2}\Delta \mathbf{V} \cdot \nabla \mathbf{V}^j\right) - \Delta t L^{j+1/2}(\Delta \mathbf{V}) + \nabla \cdot \Pi_i(\Delta \mathbf{V}) \\ = \mathbf{J}^{j+1/2} \times \mathbf{B}^{j+1/2} - m_i n^{j+1/2}\mathbf{V}^j \cdot \nabla \mathbf{V}^j - \nabla p^{j+1/2} - \nabla \cdot \Pi_i\left(\mathbf{V}^j\right) \end{aligned} \tag{1}$$

$$\frac{\Delta n}{\Delta t} + \frac{1}{2}\mathbf{V}^{j+1} \cdot \nabla \Delta n = -\nabla \cdot \left(\mathbf{V}^{j+1} \cdot n^{j+1/2}\right) \tag{2}$$

$$\begin{aligned} \frac{3n}{2}\left(\frac{\Delta T_\alpha}{\Delta t} + \frac{1}{2}\mathbf{V}_\alpha^{j+1} \cdot \nabla \Delta T_\alpha\right) + \frac{1}{2}\nabla \cdot \mathbf{q}_\alpha(\Delta T_\alpha) \\ = -\frac{3n}{2}\mathbf{V}_\alpha^{j+1} \cdot \nabla T_\alpha^{j+1/2} - n T_\alpha^{j+1/2}\nabla \cdot \mathbf{V}_\alpha^{j+1} - \nabla \cdot \mathbf{q}_\alpha\left(T_\alpha^{j+1/2}\right) + Q_\alpha^{j+1/2} \end{aligned} \tag{3}$$

$$\frac{\Delta\mathbf{B}}{\Delta t}+\frac{1}{2}\mathbf{V}^{j+1}\cdot\nabla\Delta\mathbf{B}+\frac{1}{2}\nabla\times\frac{1}{ne}\left(\mathbf{J}^{j+1/2}\times\Delta\mathbf{B}+\Delta\mathbf{J}\times\mathbf{B}^{j+1/2}\right)+\frac{1}{2}\nabla\times\eta\Delta\mathbf{J}$$
$$=-\nabla\times\left[\frac{1}{ne}\left(\mathbf{J}^{j+1/2}\times\mathbf{B}^{j+1/2}-\nabla p_e\right)-\mathbf{V}^{j+1}\times\mathbf{B}^{j+1/2}+\eta\mathbf{J}^{j+1/2}\right] \tag{4}$$

where superscripts show the time-level indices, and Δ indicates the change from a single step. The charge current density is directly related to magnetic field, $\mu_0\mathbf{J}=\nabla\times\mathbf{B}$, the number density is the same for the two species (α=i,e), and m_i is the ion mass. The ion flow velocity ($\mathbf{V}_\mathrm{i}$) is equivalent to the plasma flow velocity, while the electron flow velocity is $\mathbf{V}_\mathrm{e}=\mathbf{V}-\mathbf{J}/ne$. The pressure p (without subscript) is the sum of the electron and ion pressures, $n(T_\mathrm{e}+T_\mathrm{i})$, and the differential operator L in (1) is the linear MHD force operator,

$$L(\Delta\mathbf{V})=\frac{1}{\mu_0}\left\{\nabla\times\left[\nabla\times(\Delta\mathbf{V}\times\mathbf{B})\right]\right\}\times\mathbf{B}+\mathbf{J}\times\nabla\times(\Delta\mathbf{V}\times\mathbf{B})+\nabla\left(\Delta\mathbf{V}\cdot\nabla p+\frac{5}{3}p\nabla\cdot\Delta\mathbf{V}\right).$$

Heating in (3) for each species appears as the term Q_α, and η is the electrical resistivity. The number density appearing in (3) and (4), may be averaged from the j+1/2 and j+3/2 time-levels, since both values are available. However, the j+1 level of electron flow in the electron temperature advance is not known until after the magnetic advance, so (3) may be solved first without the updated $\mathbf{V}_\mathrm{e}$ to predict p_e for (4), followed by a correction of electron temperature with the updated $\mathbf{V}_\mathrm{e}$.

Important drift effects from finite-sized gyro-orbits appear in (1), (3), and (4). In the flow velocity evolution (1), they result from the gyroviscous part of the traceless stress tensor, Π_i, and for the Braginskii model, the gyroviscous stress is

$$\Pi_{gv}=\frac{m_i p_i}{4eB}\left[\hat{\mathbf{b}}\times\mathbf{W}\cdot\left(\mathbf{I}+3\hat{\mathbf{b}}\hat{\mathbf{b}}\right)-\left(\mathbf{I}+3\hat{\mathbf{b}}\hat{\mathbf{b}}\right)\cdot\mathbf{W}\times\hat{\mathbf{b}}\right],\qquad\left(\mathbf{W}\equiv\nabla\mathbf{V}+\nabla\mathbf{V}^T-\frac{2}{3}\mathbf{I}\nabla\cdot\mathbf{V}\right)$$

where $\hat{\mathbf{b}}\equiv\mathbf{B}/B$. The heat flux vectors $\mathbf{q}_\alpha$ for separate species temperatures contain a term that directs heat perpendicular to both the magnetic field and the temperature gradient, $+2.5p_\mathrm{i}(eB)^{-1}\hat{\mathbf{b}}\times\nabla T_\mathrm{i}$ for ions and $-2.5p_\mathrm{e}(eB)^{-1}\hat{\mathbf{b}}\times\nabla T_\mathrm{e}$ for electrons. In (4), the terms associated with drifts appear explicitly. Finite ion pressure leads to an imbalance between the Lorentz force and the electron pressure gradient, which causes magnetic perturbations to drift.

To ensure that the algorithm is numerically stable, the drift terms are being implemented implicitly, as indicated in (1)-(4). At present, NIMROD's linear drift effects include the Hall and diamagnetic effects in the magnetic advance, gyro-viscosity (except for contributions from equilibrium flow) in the velocity advance, and the cross-heat flux terms in separate electron and ion temperature advances. After completing drift effects

associated with equilibrium flow, we will also need to implement matrix-free dot-product routines for nonlinear 3D computations.

We have begun preliminary applications of extended MHD model described in the preceding paragraphs to the equilibria shown in Figure 2. The first application was to the $T_{ped} = 600$ eV equilibrium. Conventional wisdom holds that these effects are stabilizing at high-*n*, and are often cited as the reason that high-*n* modes are not observed in experiments. However, we have found that drift effects have little consequence for the linear growth rate for this case, even up to $n = 40$. The MHD growth rate is $\gamma = 7.6 \times 10^5$ sec^{-1}. With two-fluid and FLR effects, this is slightly reduced to $\gamma = 6.5 \times 10^5$ sec^{-1}, with a real frequency of $\omega = 5.4 \times 10^5$ sec^{-1}. The eigenfunction for the two case is illustrated in Figure 7.

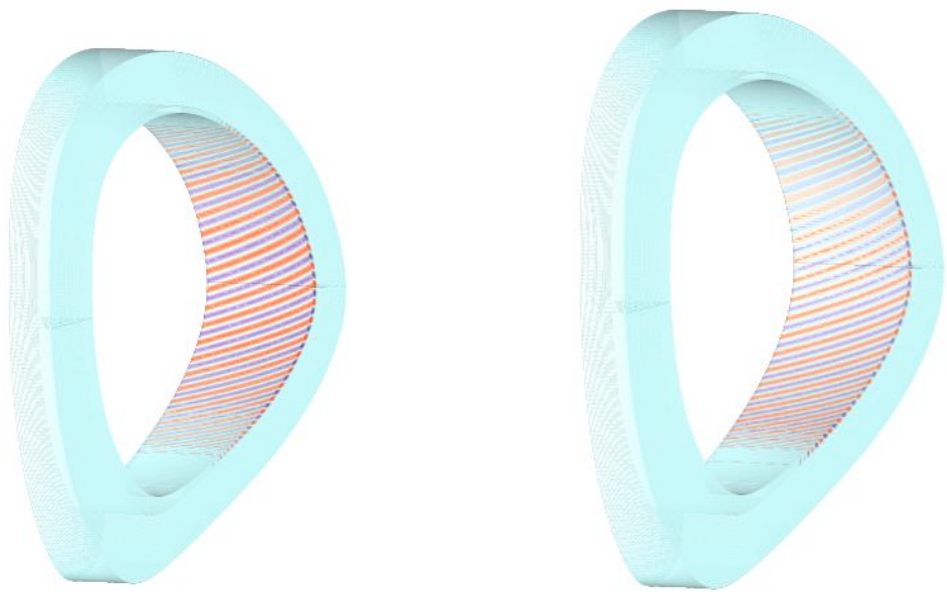

Figure 7. Edge localized eigenmode for $n = 40$. The inside of the discharge has been removed to reveal the edge structure. The figure on the left is with the resistive MHD model. The figure on the right is with the extended MHD model including Hall, diamagnetic, and gyro-viscous (FLR) terms. While there is a small but quantitative difference in the growth rate, the only significant difference in the structure is a slight downward shift in the figure on the right due to rotation.

One possibility for the difference between theoretical expectations and computational results in this case is the large growth rate of the MHD mode. Recall that $\gamma\tau_A = 0.36$, which is exceedingly fast. In contrast, the theoretical models usually assume that dynamical frequencies are slow compared to other characteristic frequencies, and this assumption may be violated in the present case. We are thus motivated to investigate the effect of the two-fluid and FLR effects on the growth rate for cases with lower pedestal temperature. Preliminary results of such a study are summarized in Figure 8. Here we plot the linear growth rate as a function of the toroidal mode number for the case with 400 eV pedestal temperature, for six different models: MHD, 2-fluid (Hall), and 2-

fluid/FLR (GV), for both isotropic and anisotropic ($\kappa_{\|}/\kappa_{\perp} = 10^7$) thermal diffusivity. Other parameters are the same as in Figure 5. By far the strongest stabilizing effect is provided by anisotropic thermal diffusivity.

We remark that a single, preliminary calculation for $n = 30$ with anistropic thermal diffusivity showed complete stability when the coefficient of gyro-viscosity was increased by a factor of 10. This requires further study.

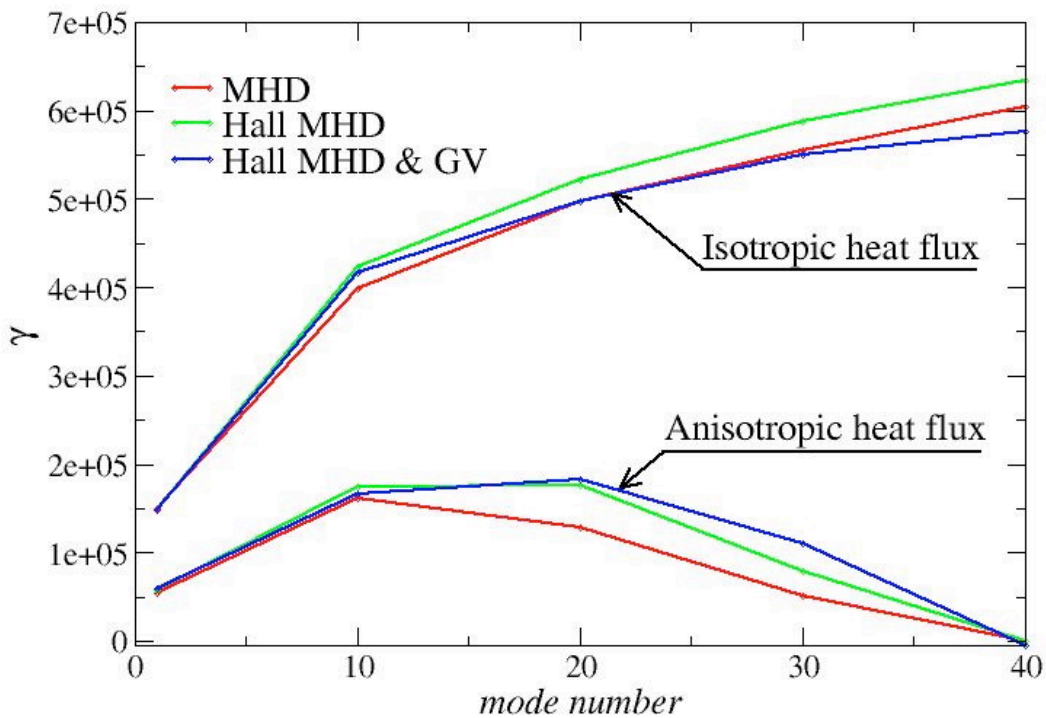

Figure 8. Linear growth rate as a function of toroidal mode number for the case of 400 eV pedestal temperature, $S = 3.7 \text{ X } 10^7$, $\text{Pr} = 10^{-3}$. Two fluid and FLR stabilization are very weak.

Some important points have been raised in these studies, as well as certain caveats. There are given below.

1. All of the linear MHD results reported here had an isotropic thermal diffusivity of $\kappa = 1 \text{ m}^2/\text{sec}$. No true ideal MHD results have been obtained. While we do not expect this effect to be qualitatively important, we have not done the calculations, and this is therefore only speculation. These calculations are underway.

2. We do not understand the nature of the internal ballooning-like mode (IM) that occurs at both high Prandtl number and low pedestal temperature. The growth rate as a function of S needs to be determined. These studies are underway.

3. For similar equilibria, the ideal MHD code ELITE generally shows a peak in the growth rate as a function of n, with the growth rate falling as n increases. In some cases there is complete stabilization at high-n. With NIMROD this behavior has only been seen with anisotropic thermal diffusivity; it has never been seen with ideal MHD, or even with isotropic thermal diffusivity. The reason for this discrepancy is unknown, but the results reported here should be viewed in this context.

4. The NIMROD results reported for high-n (up to $n = 40$) should not be considered as spatially converged. In fact, there is a reasonable expectation that they are not, and that the converged results could differ significantly (even qualitatively) from those presented here. In particular, it is possible that, for highly anisotropic thermal diffusivity, spatial discretization errors could bleed a small amount of parallel transport into perpendicular transport, thus providing a stabilizing effect that could account for the behavior shown in Figure 5. These convergence studies are underway.

5. High-n modes require significantly more poloidal spatial resolution that low-n modes. Thus, non-linear calculations with 20 to 40 toroidal modes may require significantly more spatial resolution than was previously assumed. It all depends the importance of the high-n modes (see #6, below).

6. Meaningful non-linear calculations cannot be performed if there is no stabilization of the high-n modes. This is because the energy spectrum will become flat and the calculation will lose toroidal resolution. So far, we have not found any reliable stabilization mechanism. It is hoped that a two-fluid Ohm's law, FLR effects (gyro-viscosity), and anisotropic thermal diffusivity will become more effective stabilization mechanisms at lower pedestal temperature, where the linear MHD growth rate is lower, but this remains to be seen. *If physical high-n stabilization is not found, it is unlikely that we will be able to meet the non-linear calculation requirements of the fourth quarter milestone without compromising scientific integrity*.